Progress In Electromagnetics Research B, Vol. 69, 31–45, 2016

Suspension Force Modeling and Electromagnetic Characteristics Analysis of an Interior Bearingless Permanent Magnet Synchronous Motor

Xiaodong Sun[1, 2, *], Shuai Luo[2], Long Chen[1, 2], Ruoyu Zhao[3], and Zebin Yang[3]

Abstract—Interior bearingless permanent magnet synchronous motors (IBPMSMs) are a new type of machines having two sets of windings in the stator, offering no lubrication and no mechanical friction, high efficiency, robust rotor construction, hybrid torque production nature and flux-weakening capability. In this paper, the suspension force modeling and the static electromagnetic characteristics of an IBPMSM are studied. The suspension force model of the IBPMSM is established and investigated based on the Maxwell tensor method. And then the static electromagnetic characteristics, including permanent magnet (PM) flux linkage, EMF, inductances, electromagnetic torque and suspension force, are discussed with the finite element analysis (FEA) method. The electromagnetic characteristics of the IBPMSM are very helpful for the design and optimization of the motor. The effectiveness of the proposed suspension force mathematical model is verified by comparing the theoretical results with FEA-based predictions. The work in this paper lays an important foundation for the optimization design and control strategies of the IBPMSM.

1. INTRODUCTION

Bearingless motors are a new type of motors, which combine the functions of traditional motors and magnetic bearings. It overcomes not only the defects of friction and thermal problems in traditional mechanical bearings, but also the problem of high cost and complex of magnetic bearing system [1–3]. Compared with the ordinary motors, the bearingless motor only needs to add a set of suspension windings. Owing to the small size, long life, high speed, no lubrication and no mechanical friction, the bearingless motors are attractive for some special environments, such as aeronautics, bio-engineering, laser scanning, flywheel energy storage system, etc. [4–6].

Bearingless motors have been widely researched since they appeared. Recently, many kinds of bearingless motors have been studied, including bearingless induction motors [7, 8], bearingless switched reluctance motors [9, 10], bearingless permanent magnet synchronous motors (BPMSMs), etc. The BPMSM has been widely studied owing to its compact structure, high efficiency, high power factor, small size and superior controlled characteristics, showing great research values [11–13]. In [14], a suspension force mathematical model of BPMSMs is presented based on the magnetic circuit inductance model and virtual displacement principle. The mathematical model has a characteristic of high accuracy. However, the mathematical model is too complicated in calculation. In [15], a suspension force mathematical model of the bearingless switched reluctance motors is built with Maxwell stress tensor method. The mathematical model is simple, and the result of the experiment shows that the mathematical model is effective.

Received 19 May 2016, Accepted 12 July 2016, Scheduled 26 July 2016

* Corresponding author: Xiaodong Sun (xdsun@ujs.edu.cn).

[1] School of Automobile and Traffic Engineering, Jiangsu University, No. 301, Xuefu Road, Zhenjiang, Jiangsu 212013, China.

[2] Automotive Engineering Research Institute, Jiangsu University, No. 301, Xuefu Road, Zhenjiang, Jiangsu 212013, China. [3] School of Electrical and Information Engineering, Jiangsu University, No. 301, Xuefu Road, Zhenjiang, Jiangsu 212013, China.

This paper is devoted to the study of the suspension force modeling and electromagnetic characteristics of an interior bearingless permanent magnet synchronous motor (IBPMSM), which is helpful for the optimization design and control strategies of the motor. Hence, Section 2 of this paper introduces the suspension principle, then the suspension force model of the IBPMSM according to the Maxwell stress tensor method is established. Thereafter, in Section 3, the permanent magnet (PM) flux linkage is studied firstly since it has great impact on EMF, inductance, and electromagnetic torque. Then, harmonic analysis to EMF is presented. Moreover, the three-phase inductance and d-q axis inductance of the torque winding, and the electromagnetic torque and cogging torque are analyzed. At last, the suspension force mathematical model is verified by finite element analysis (FEA) [16]. Conclusion is drawn in Section 4.

2. SUSPENSION FORCE MODELING

The torque winding and PMs generate the torque magnetic field, and the suspension winding generates suspension magnetic field having different numbers of pole-pairs with torque magnetic field. The suspension magnetic field breaks the symmetrical balanced torque magnetic field, which causes one side of the magnetic field enhanced and the other reduced. Hence, the suspension force along the enhanced side is produced. The premise of generating a stable suspension force is that the pole-pair numbers of torque windings pole pairs P_M and suspension windings pole pairs P_S are consecutive, i.e., $P_M = P_S \pm 1$.

Figure 1 shows the principle of the suspension force generation. The four-pole magnetic field Ψ_4 is generated by torque windings and PMs, and the six-pole magnetic field Ψ_6 is generated by the suspension windings. In Fig. 1(a), when the suspension winding $N_{S\alpha}$ is excited, the suspension winding magnetic field Ψ_6 and torque winding magnetic field Ψ_4 keep the same rotation directions in x-axis positive directions, thus the magnetic field along x-axis positive directions is strengthened. However, the two magnetic fields are in opposite directions in the x-axis negative directions, which causes the magnetic field decreased in the x-axis negative directions. Therefore, the suspension force F_x along x-axis positive directions can be generated. Similarly in Fig. 1(b), the suspension force F_y along y-axis positive directions can be produced by the suspension force winding current in the suspension winding $N_{S\beta}$.

The suspension force model of the IBPMSM is built based on the Maxwell tensor method as follows. The three-phase torque windings currents i_{AM}, i_{BM}, and i_{CM}, and suspension winding currents i_{AS},

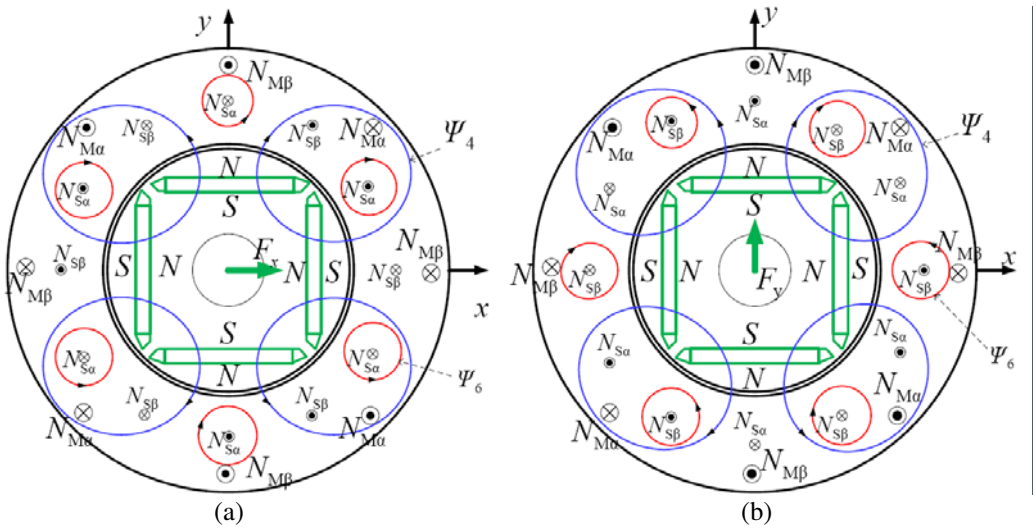

Figure 1. Principle of suspension force generation. (a) Suspension force F_x. (b) Suspension force F_y.

i_{BS}, and i_{CS} can be expressed as

$$\begin{cases} i_{AM} = I_M \cos(\omega t + \theta_M) \\ i_{BM} = I_M \cos(\omega t - 120^\circ + \theta_M) \\ i_{CM} = I_M \cos(\omega t + 120^\circ + \theta_M) \end{cases} \tag{1}$$

$$\begin{cases} i_{AS} = I_S \cos(\omega t + \theta_S) \\ i_{BS} = I_S \cos(\omega t - 120^\circ + \theta_S) \\ i_{CS} = I_S \cos(\omega t + 120^\circ + \theta_S) \end{cases} \tag{2}$$

where ω is the current angular velocity; I_M and I_S are the current magnitudes of the torque winding and suspension winding currents, respectively; θ_M and θ_S are the initial angle of torque winding current and suspension winding current, respectively.

Without considering the magnetic saturation, the Maxwell force acting on the rotor surface F_P can be expressed as [17]

$$dF_P = \frac{B^2(\varphi, t)\, dS}{2\mu_0} \tag{3}$$

The suspension force along x-axis and y-axis can be written as

$$\begin{cases} dF_x = \dfrac{B^2(\varphi, t)\, dS}{2\mu_0} \cos\varphi = \dfrac{B^2(\varphi, t)\, lr}{2\mu_0} \cos\varphi d\varphi \\ dF_y = \dfrac{B^2(\varphi, t)\, dS}{2\mu_0} \sin\varphi = \dfrac{B^2(\varphi, t)\, lr}{2\mu_0} \sin\varphi d\varphi \end{cases} \tag{4}$$

$$B(\varphi, t) = B_{M1}(\varphi, t) + B_S(\varphi, t) + B_{M2}(\varphi, t) \tag{5}$$

where $B(\varphi, t)$ is the airgap flux density, μ_0 the permeability in the vacuum, S the rotor surface area, l the effective rotor length, r the rotor outer surface radius, and φ the mechanical angle of rotor that has rotated. $B_{M1}(\varphi, t)$, $B_S(\varphi, t)$ and $B_{M2}(\varphi, t)$ are the torque winding airgap flux density, suspension winding airgap flux density and PM airgap flux density, respectively, which can be expressed as

$$\begin{cases} B_S(\varphi, t) = \mu_0 \dfrac{F_S}{\delta} \cos(\omega t - p_S\varphi - \theta_S) \\ B_{M1}(\varphi, t) = \mu_0 \dfrac{F_{M1}}{\delta} \cos(\omega t - p_M\varphi - \theta_M) \\ B_{M2}(\varphi, t) = \mu_0 \dfrac{F_{M2}}{\delta} \cos(\omega t - p_M\varphi - \theta_P) \end{cases} \tag{6}$$

where the F_S, F_{MI} and F_{M2} are suspension windings, torque windings and the PM airgap Magneto-Motive Force (MMF), respectively; P_M and P_S are the pole pairs of torque windings and suspension windings, respectively; θ_p is the initial phase angle of PM MMF.

Since the magnetic field generated by the PMs and torque windings are both four-pole magnetic fields with the same frequency, the two MMFs can be superposed. Fig. 2 shows the superposed MMF produced by the PMs and the torque windings. The airgap flux density $B_{PM}(\varphi, t)$ synthesized by torque windings and PMs can be expressed as

$$B_{PM}(\varphi, t) = \mu_0 \frac{F_{PM}}{\delta} \cos(\omega t - p_M\varphi - \theta_{PM}) \tag{7}$$

where F_{PM} and θ_{PM} are the synthesized MMF and the initial phase angle of the synthesized MMF, respectively. From Fig. 2, we can get

$$\begin{cases} I_{PM} = I_P^2 + I_M^2 + I_P I_M \cos(\theta_P - \theta_M) \\ \theta_{PM} = \arctan\left(\dfrac{I_P \sin\theta_P + I_M \sin\theta_M}{I_P \cos\theta_P + I_M \cos\theta_M}\right) \end{cases} \tag{8}$$

where I_{PM} is the equivalent current which produced by F_{PM}, and I_p is the equivalent current of the PM. Finally, the airgap flux density can be expressed as

$$B(\varphi, t) = B_S(\varphi, t) + B_{PM}(\varphi, t) \tag{9}$$

As shown in Fig. 3, δ_0 is the airgap length when the rotor stays at the center of the motor, and δ is the airgap length when the rotor is eccentric. From Fig. 3, we can get

$$\delta = \delta_0 - e\cos(\varphi - \varphi_0) = \delta_0\left(1 - \frac{e}{\delta_0}\cos(\varphi - \varphi_0)\right) \tag{10}$$

$$\frac{1}{\delta} \approx \frac{1}{\delta_0}\left(1 + \frac{e}{\delta_0}\cos(\varphi - \varphi_0)\right) \tag{11}$$

$$\begin{cases} x = e\cos\varphi_0 \\ y = e\sin\varphi_0 \end{cases} \tag{12}$$

where φ_0 is the angle between the rotor eccentricity directions and the x-axis; x and y are the rotor eccentric distance in x-axis and y-axis, respectively; e is the total rotor eccentric distance. Combining formulas (6), (7), (9) and (10), we can get

$$\begin{cases} B_S(\varphi,t) = B_{S1}\left(1 + \dfrac{e}{\delta_0}\cos(\varphi - \varphi_0)\right)\cos(\omega t - p_S\varphi - \theta_S) \\ B_{PM}(\varphi,t) = B_{PM1}\left(1 + \dfrac{e}{\delta_0}\cos(\varphi - \varphi_0)\right)\cos(\omega t - p_M\varphi - \theta_{PM}) \end{cases} \tag{13}$$

Define

$$\begin{cases} B_{S1} = \mu_0\dfrac{F_S}{\delta_0} \\ B_{PM1} = \mu_0\dfrac{F_{PM}}{\delta_0} \end{cases} \tag{14}$$

$$\tau = \frac{e}{\delta_0} \tag{15}$$

where F_S and F_{PM} can be expressed as

$$\begin{cases} F_S = \dfrac{3}{2}\dfrac{4}{\pi}\dfrac{\sqrt{2}}{2}\dfrac{N_S I_S k_{dS}}{p_S} \\ F_{PM} = \dfrac{3}{2}\dfrac{4}{\pi}\dfrac{\sqrt{2}}{2}\dfrac{N_M I_{PM} k_{dM}}{p_M} \end{cases} \tag{16}$$

where N_S and N_M are the number of suspension windings and torque windings coils per phase, respectively, and k_{ds} and k_{dM} are the torque winding and suspension winding stacking coefficients, respectively.

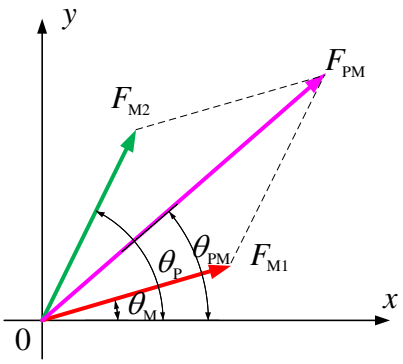

Figure 2. The MMF synthesized by torque winding.

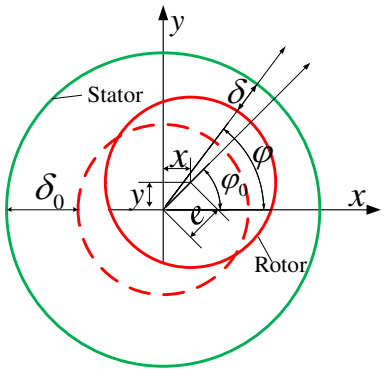

Figure 3. Airgap length.

Combining Equations (4), (9), (13), and (15), we can get:

$$\begin{aligned} F_x &= \frac{\pi lrB_{PM1}B_{S1}\cos(\theta_M-\theta_S)}{2\mu_0}+\frac{\pi\tau lr(B_{PM1}^2+B_{S1}^2)\cos\varphi_0}{2\mu_0} \\ &\quad +\frac{\pi\tau^2 lrB_{PM1}B_{S1}\cos(\theta_M-2\varphi_0-\theta_S)}{8\mu_0}+\frac{\pi\tau^2 lrB_{PM1}B_{S1}\cos(\theta_M-\theta_S)}{4\mu_0} \end{aligned} \tag{17}$$

$$\begin{aligned} F_y &= \frac{\pi lrB_{PM1}B_{S1}\sin(\theta_M-\theta_S)}{2\mu_0}+\frac{\pi\tau lr(B_{PM1}^2+B_{S1}^2)\sin\varphi_0}{2\mu_0} \\ &\quad -\frac{\pi\tau^2 lrB_{PM1}B_{S1}\sin(\theta_M-2\varphi_0-\theta_S)}{8\mu_0}+\frac{\pi\tau^2 lrB_{PM1}B_{S1}\sin(\theta_M-\theta_S)}{4\mu_0} \end{aligned} \tag{18}$$

The values of τ and B_{S1} are too negligible and can be ignored when the motor is working, thus the formula with τ^2 and B_{S1}^2 can be omitted, and formulas (17) and (18) can be simplified as:

$$F_x=\frac{\pi lrB_{PM1}B_{S1}\cos(\theta_M-\theta_S)}{2\mu_0}+\frac{\pi\tau lrB_{PM1}^2\cos\varphi_0}{2\mu_0} \tag{19}$$

$$F_y=\frac{\pi lrB_{PM1}B_{S1}\sin(\theta_M-\theta_S)}{2\mu_0}+\frac{\pi\tau lrB_{PM1}^2\sin\varphi_0}{2\mu_0} \tag{20}$$

When combining Equations (12), (14), (15) and (16) into Equations (19) and (20), the following expression can be obtained

$$F_x=k_aI_SI_{PM}\cos(\theta_M-\theta_S)+k_bx \tag{21}$$

$$F_y=k_aI_SI_{PM}\sin(\theta_M-\theta_S)+k_by \tag{22}$$

where $k_a=\frac{3lr\mu_0N_SN_Mk_{dS}k_{dM}}{4\pi\delta_0^2}$, and $k_b=\frac{9\mu_0lrN_M^2I_{PM}^2k_{dM}^2}{8\pi\delta_0^3}$. From Equations (21) and (22), we can get the conclusion that the suspension force in the IBPMSM is mainly composed by two parts. The first part is the Maxwell force generated by two windings. It is clear that the first part is proportional to the suspension windings current, equivalences torque windings current, and the cosine of two windings phase angle. The second part emerges when the rotor is off-center, and proportional to the eccentric distance.

3. STATIC ELECTROMAGNETIC CHARACTERISTIC ANALYSIS

In this part, the finite element model and static electromagnetic characteristics including PM flux linkage, EMF, inductance, electromagnetic torque and the suspension force of the IBPMSM will be presented.

Figure 4 shows the finite element model of the IBPMSM. The motor consists of four-pole torque windings, six-pole suspension windings, stator, rotor, PMs, shaft and aluminum. The dimensions of the prototype are shown in Table 1. Furthermore, the mesh plot of the FEA model is shown in Fig. 5. The denser the gap mesh is, the more accurate the calculation becomes. It can be seen that the gap mesh is denser than other parts.

Figure 6 shows the magnetic density distribution of the IBPMSM. From Fig. 6, it can be seen that the PM and torque winding produce four-pole magnetic field in Figs. 6(a) and (b), respectively, and the suspension winding produces six-pole magnetic field in Fig. 6(c). Moreover, the synthesized magnet density produced by PMs, torque windings and suspension windings is shown in Fig. 6(d). It is obvious that the magnetic density in right side is larger than that of the left side.

3.1. PM Flux Linkage and EMF

Figure 7 shows the PM flux linkage when the rotor rotates one round. From Fig. 7, taking phase A as an example, it can be seen that the flux linkage transforms two cycles in a mechanical angle cycle and shifts 60 mechanical degrees (i.e., 120 electrical degrees) to phase B (or phase C). Since the PM flux linkage has a great influence on other performance of the motor, harmonic analysis of the PM flux

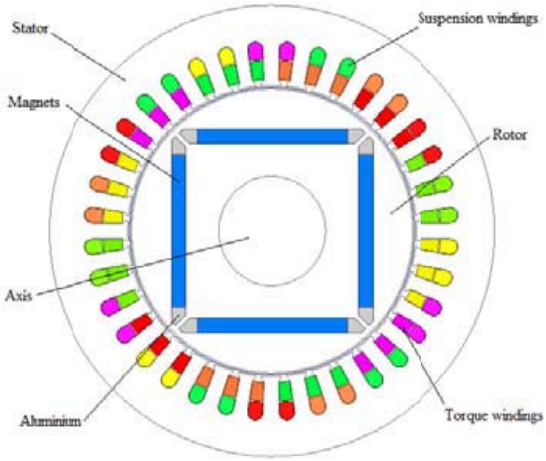

Figure 4. Prototype motor.

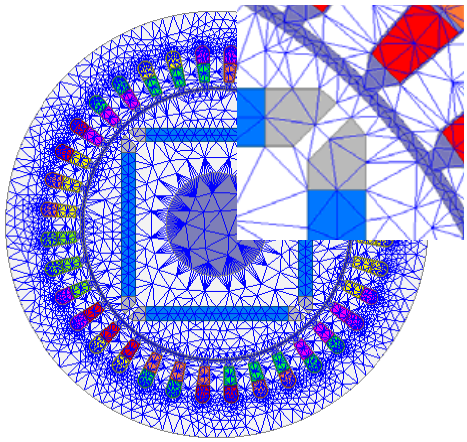

Figure 5. Mesh plot.

Table 1. Specification of the prototype machine.

Parameter	Symbol	Value
Stator		
Stator material	-	DW360_50
Stator outer diameter	R_s	124 mm
Stator slot number	Q	36
Pole pairs of torque windings	P_M	2
Pole pairs of suspension windings	P_S	3
Turns of torque windings per slot	N_M	40
Turns of suspension windings per slot	N_S	25
Number of winding parallel ways	A	1
Airgap length	δ_0	1 mm
Stator length	l	80 mm
Rotor		
Rotor material	-	DW360_50
Rotor diameter	R	78 mm
Permanent magnetic material	-	NdFe35
Coercive force	H_C	-890 KA/m
Magnet remanence at 20°C	B_r	1.099 T
Magnet thickness	H	4 mm

linkage is needed. The FFT analysis of phase A PM flux linkage in an electrical period is shown in Fig. 8. From Fig. 8, it can be seen that the harmonic only accounts for a small part. Moreover, the first to eleventh orders of the odd harmonic amplitude are shown in Fig. 9. It can be seen from Fig. 9 that the ratio of the total high order harmonic values and fundamental values is only 7.4% in the IBPMSM, and the third order harmonic accounts for 85.7% of the total harmonics. Without considering the high order harmonics, the three-phase PM flux linkage Ψ_{PMA}, Ψ_{PMB}, and Ψ_{PMC} can be written as

$$\begin{cases} \Psi_{PMA} = \Psi_M \cos(P_M\varphi) \\ \Psi_{PMB} = \Psi_M \cos(P_M\varphi - 120°) \\ \Psi_{PMC} = \Psi_M \cos(P_M\varphi + 120°) \end{cases} \tag{23}$$

where Ψ_M is the amplitude of the fundamental wave of the PM flux linkage.

The EMF is easily obtained when the PM flux linkage is known, and their relationships can be

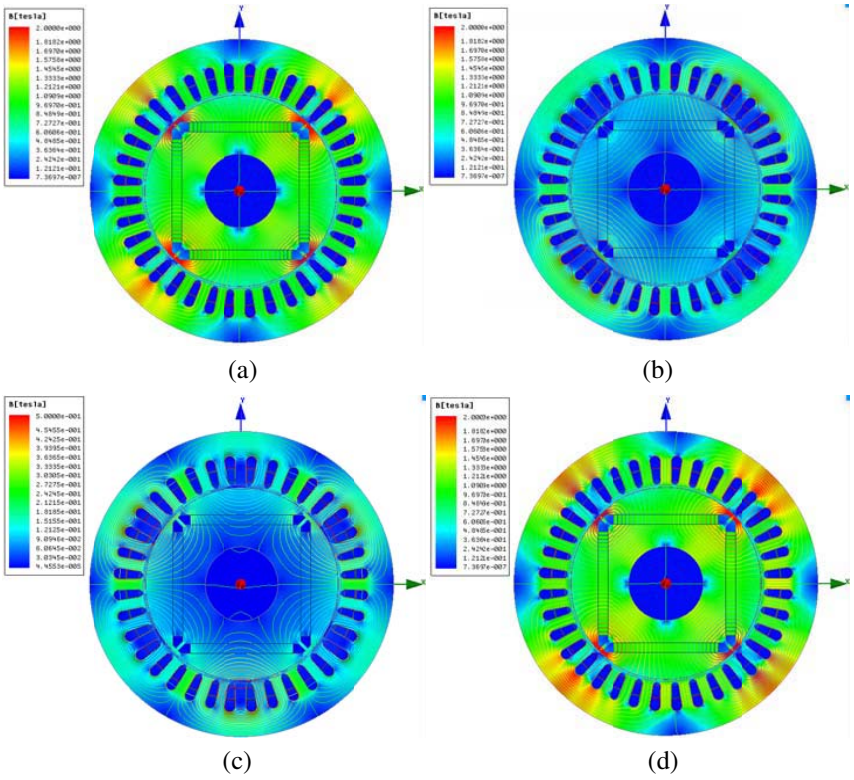

Figure 6. Magnetic density distribution of the IBPMSM. (a) Magnetic density of the PMs. (b) Magnetic density of the torque windings (3A). (c) Magnetic density of the suspension windings (2A). (d) Magnetic density of the PMs and two sets of windings.

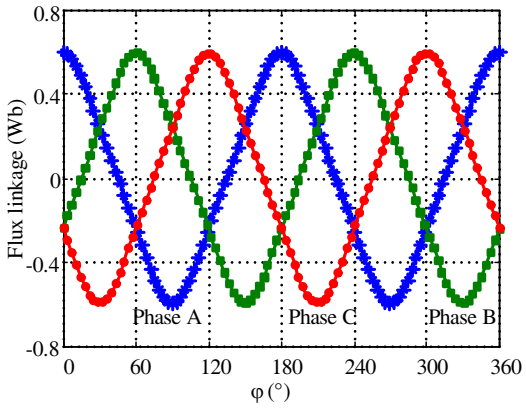

Figure 7. PM flux linkage.

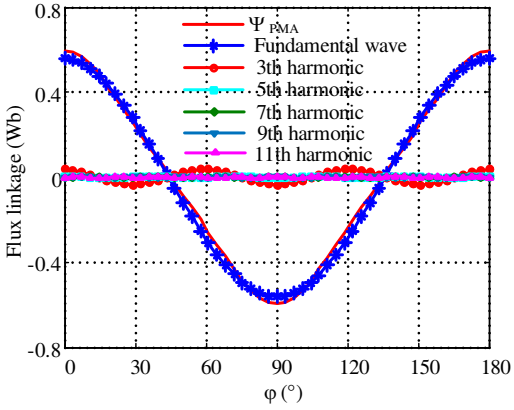

Figure 8. Ψ_{PMA} FFT analysis.

expressed as

$$e = \frac{d\Psi_{PM}}{dt} = \frac{d\Psi_{PM}}{d\theta} \cdot \frac{2\pi n}{60} \tag{24}$$

where e is the EMF, Ψ_{PM} the PM flux linkage, θ the electrical angle of rotor which can be expressed as $\theta = P_M * \varphi$, and n the speed of the motor.

Figure 10 shows the EMF waveforms of the IBPMSM at the speed of 3000 r/min, which are given according to Equation (24). It can be seen from Fig. 10 that the characteristics of EMF waveforms are the same as the PM flux linkage in pole pairs and mechanical degrees shifted between phases, except

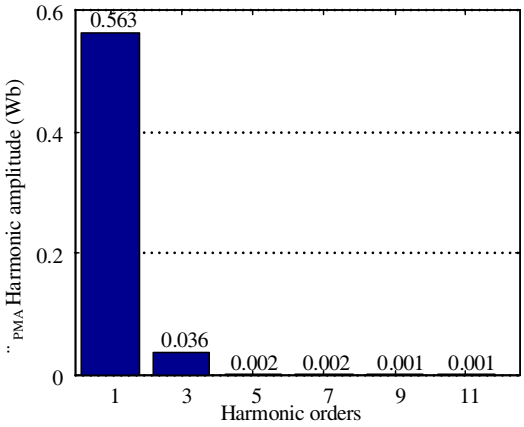

Figure 9. Amplitude of the fundamental wave and the high order harmonics of the Ψ_{PMA}.

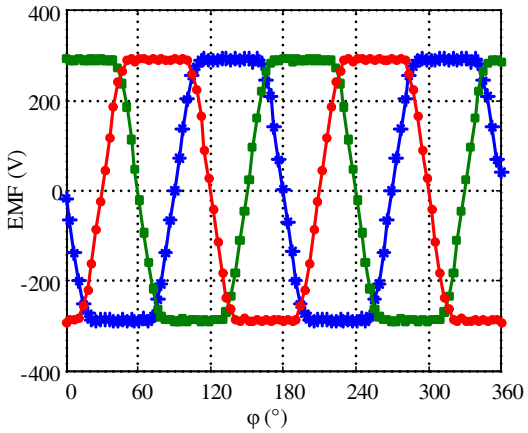

Figure 10. EMF waveforms.

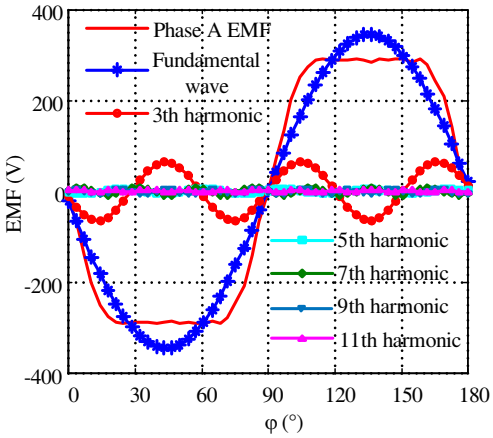

Figure 11. Phase A EMF FFT analysis.

that phase lags behind 45 mechanical degrees (i.e., 90 electrical degrees). Fig. 11 shows the FFT analysis result of phase A EMF waveforms in a electrical period. Fig. 12 shows the amplitude of fundamental waveforms and high order harmonics of the EMF. It can be seen from Figs. 11 and 12 that the ratio of the total high orders harmonic values and fundamental values is 25%, and the third order harmonic amplitude is much larger than that of any other high order harmonics. The main reason is that the PM flux linkage third order harmonic is large.

3.2. Inductance

Inductance is the ability of unit current produces flux linkage. Taking phase A as an example, when phase A winding current i_A is excited, the phase A winding self-inductance L_{aa} and the mutual inductance between phase A and phase B, phase C M_{ba} and M_{ca} can be expressed as

$$\begin{cases} L_{aa} = \dfrac{\Psi_A - \Psi_{PMA}}{i_A} \\ M_{ba} = \dfrac{\Psi_B - \Psi_{PMB}}{i_A} \\ M_{ca} = \dfrac{\Psi_C - \Psi_{PMC}}{i_A} \end{cases} \tag{25}$$

where Ψ_A, Ψ_B, and Ψ_C are respectively the phase A, phase B, and phase C flux linkages produced by the permanent and phase A winding current i_A.

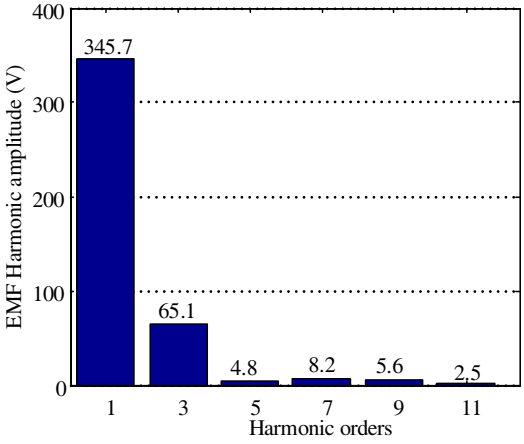

Figure 12. Amplitude of the fundamental wave and the high order harmonics of the EMF.

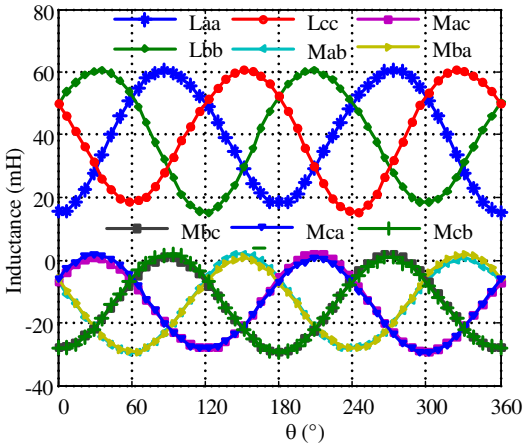

Figure 13. Torque winding three phase inductance.

The suspension winding current is zero when the torque winding inductance is studied. Then, the torque winding inductance can be calculated according to Equation (25). The data of PM flux linkage and the synthetic flux linkage produced by PMs and torque winding current are obtained with the help of the software Ansoft Maxwell. Fig. 13 shows the torque winding inductance. In an electrical period (i.e., $\theta = 0$ to 2π), taking phase A as an example, when $\theta = 0$, the magnetic field produced by phase A winding current will enhance the PM magnetic field. Thus, the saturation is more obvious, and the minimum inductance values appear. When $\theta = \pi$, phase A magnet magnetic field will weak the PM magnetic field, which results in weaken saturation, and the inductance values are larger than the inductance ones when $\theta = 0$. When $\theta = \pi/2$ or $\theta = 3\pi/2$, the phase A magnetic field is not affected by PM magnetic field, so the phase A magnetic field is not saturated, and the inductance peak values appear. From Fig. 13, it can also be seen that the mutual inductance M_{ab} is equal to M_{ba}, M_{ac} equal to M_{ca}, and M_{bc} equal to M_{cb}.

Figure 14 shows the result of FFT analysis of phase A self-inductance in an electrical period. From Fig. 14, it can be seen that the high order harmonics are too small compared with the fundamental wave. Furthermore, the amplitude of the fundamental wave and the high order harmonics of the phase A self-inductance is shown in Fig. 15. The high order harmonics only account for 5% of the fundamental wave amplitude. Hence, the high order harmonics can be neglected.

Generally, in order to model and control IBPMSM, the rotor coordinate system (i.e., d-q coordinate

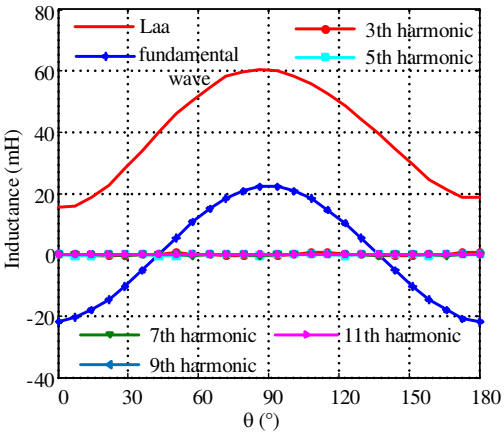

Figure 14. *L*aa FFT analysis.

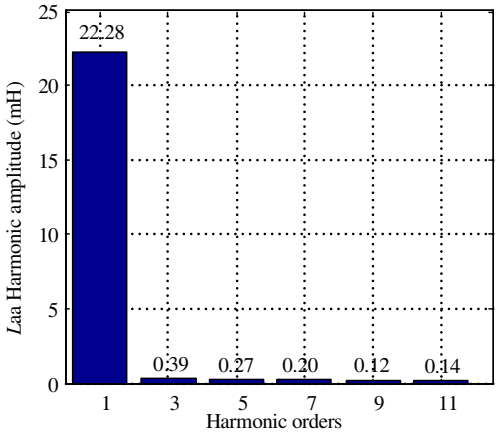

Figure 15. Amplitude of the fundamental wave and the high order harmonics of *L*aa.

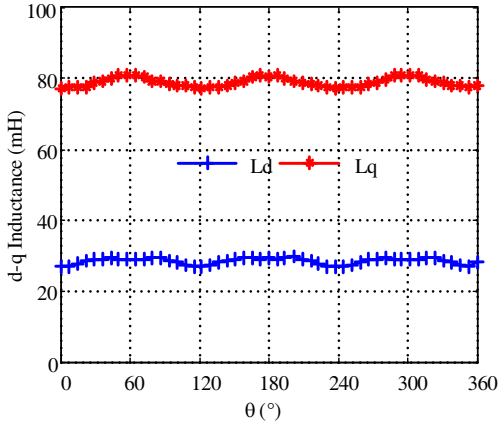

Figure 16. Torque winding *d*-*q* axis inductance.

system) is widely used. The *d*-*q* axis inductance L_{dq0} can be calculated as follows

$$L_{dq0} = \mathbf{C}\mathbf{L}_{abc}\mathbf{C}^T \tag{26}$$

$$\mathbf{C} = \frac{2}{3}\begin{bmatrix} \cos(\theta) & \cos(\theta - 2\pi/3) & \cos(\theta + 2\pi/3) \\ -\sin(\theta) & -\sin(\theta - 2\pi/3) & -\sin(\theta + 2\pi/3) \\ 1/2 & 1/2 & 1/2 \end{bmatrix} \tag{27}$$

where the $\mathbf{C}$ is the transformation matrix, $\mathbf{L}_{abc}$ the three phase inductance, and $\mathbf{C}^T$ the transpose of $\mathbf{C}$.

Figure 16 shows the torque winding *d*-*q* inductance. From Fig. 16, it can be seen that *q*-axis inductance L_q is much larger than *d*-axis inductance L_d. It is mainly because the magnetic permeability of the PM is much smaller than that of the rotor core, and it causes the reluctance in *d*-axis much larger than that of the *q*-axis, which is consistent with the characteristics of the salient pole PM motors.

The results of the FFT analysis of the PM flux linkage, EMF and the self-inductance are listed in Table 2.

3.3. Torque

The electromagnetic torque T_{em} of the IBPMSM can be expressed as

$$T_{em} = T_{cog} + T_{pm} + T_r \tag{28}$$

where T_{pm} is the PM torque, T_r the reluctance torque, and T_{cog} the cogging torque.

Table 2. FFT analysis results of the PM flux linkage, EMF and the self-inductance.

Items	Fundamental wave value (Peak)	Total harmonic value	Harmonic components (%)
Flux linkage (Wb)	0.563	0.042	7.4
EMF (V)	345.7	86.2	25
Self-inductance (mH)	22.28	1.12	5

3.3.1. Cogging Torque

The existence of cogging torque is the inherent characteristics of the slot motors, and it is related to the existence of the stator slots [18]. The periods of the cogging torque θ_{cog} in mechanical degrees can be expressed as

$$\theta_{cog} = \frac{360^\circ}{QM_P} \tag{29}$$

$$M_P = \frac{P_M}{HCF} \tag{30}$$

where Q is the number of stator slots, M_p the period of cogging torque, and HCF the biggest common factor between Q and P_M. In this paper, Q is equal to 36 and P_M equal to 2. According to Equations (29) and (30), it is easy to get that θ_{cog} is equal to 10. The cogging torque is shown in Fig. 17. According to Fig. 17, it can be seen that the cogging torque cycles eighteen times when the rotor rotates 180 mechanical degrees, which means that the period of the cogging torque is 10 mechanical degrees, and it is strictly consistent with the theory. It can also be seen from Fig. 17 that the average cogging toque is close to zero, which means that the cogging torque is invalid, and its existence can only cause torque ripple.

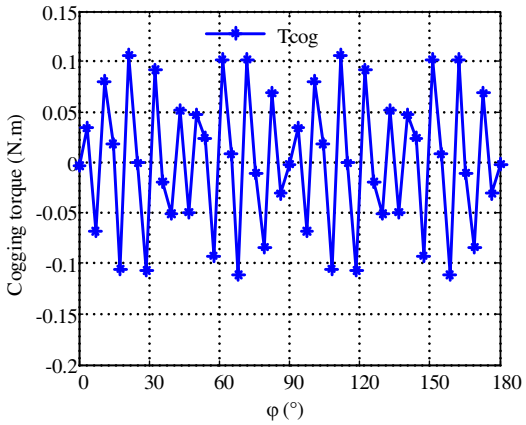

Figure 17. Cogging torque.

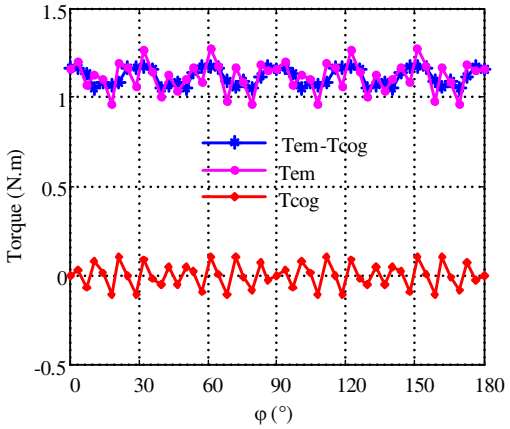

Figure 18. Electromagnetic torque.

3.3.2. PM Torque and Reluctance Torque

The PM torque and reluctance torque are effective torque. The PM torque is produced by the PMs and q-axis torque winding current, and the reluctance torque exists when inductance L_d is not equal to L_q. The PM torque and= reluctance torque can be respectively expressed as

$$T_{pm} = \frac{3}{2} P_M \Psi_{pm} i_q \tag{31}$$

$$T_r = -\frac{3}{2} P_M \left(L_d - L_q\right) i_d i_q \tag{32}$$

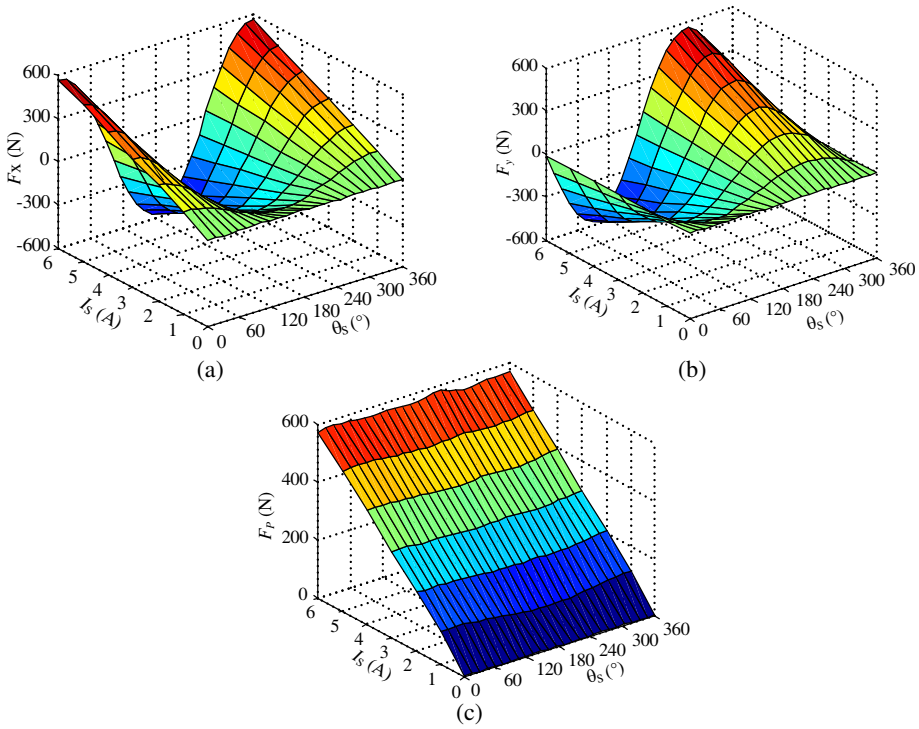

Figure 19. Suspension force versus suspension winding current and suspension winding current phase. (a) F_x versus I_S and θ_S. (b) F_y versus I_S and θ_S. (c) F_p versus I_S and θ_S.

where i_d and i_q are the equivalent currents of d-axis and q-axis, and can be written as

$$\begin{bmatrix} i_d \\ i_q \end{bmatrix} = \frac{2}{3} \begin{bmatrix} \cos\theta & \cos(\theta - 2\pi/3) & \cos(\theta + 2\pi/3) \\ -\sin\theta & -\sin(\theta - 2\pi/3) & -\sin(\theta + 2\pi/3) \end{bmatrix} \begin{bmatrix} i_{AM} \\ i_{BM} \\ i_{CM} \end{bmatrix} \tag{33}$$

Figure 18 shows the electromagnetic torque, cogging torque and effective torque (i.e., electromagnetic torque subtracts the cogging torque). From Fig. 18, we can see that the cogging torque only accounts for a very small part of the electromagnetic torque. Moreover, the effective torque is distributed as a straight line on the whole.

3.4. Suspension Force

The purpose of this part is to verify the suspension force model in the second part by FEA method. In Equations (21) and (22), the first part is the Maxwell force which is proportional to the magnitudes of suspension winding and equivalences torque winding currents, as well as the cosine of difference value of the phase angles in the two windings. The relationship among suspension force, suspension winding current and suspension winding current phase calculated by FEA software is shown in Fig. 19, where Figs. 19(a)–(c) denote the suspension force components acting on the x-axis and y-axis, and the synthetic suspension force. From Fig. 19(a), it can be seen that when suspension current is a constant value, the suspension force component F_x is changed with the change of the suspension winding current phase, and the waveform takes on a cosine distribution. When the suspension winding current phase is a certain value, the suspension force has a linear relationship with the suspension winding current. According to Fig. 19(b), it can be seen that the suspension force component F_y has the same characteristics as suspension force component F_x, except 90-degree phase difference. From Fig. 19(c), we can see that the suspension force F_P acting on the rotor increases when the suspension winding current increases, and the value of F_p is equal to the amplitude of F_x and F_y. These characteristics are in accordance with the theory analysis about the suspension force model in Section 2. Moreover, suspension force F_P does not change with the variation of suspension winding current phase. The main reason is that the

relationship among F_p, F_x, and F_y can be expressed as

$$F_p = \sqrt{\left(F_x^2 + F_y^2\right)} \tag{34}$$

Figure 20 illustrates the relationship waveforms of the suspension force and suspension windings current, and makes comparisons between the calculated and simulated suspension forces. From Fig. 20, it is obvious that the suspension force is linear with the suspension winding currents and increases when the suspension wingding current increases. In addition, the calculated suspension force has good agreement with the simulated results, although it is a little bigger due to the magnetic circuit saturation.

In Equations (21) and (22), the second part is the eccentric magnetic force which is proportional to the eccentric distance in theory. In order to avoid the influence of controllable suspension, there is no current in the suspension windings. Fig. 21 shows the relationship waveforms of the suspension force components F_x and F_y, and eccentric distance in x-axis. From Fig. 21, it can be seen that the suspension force component F_x increases when the rotor eccentric distance increases. Moreover, the relationship waveforms of the suspension force component F_x and eccentric distance in x-axis meets the proportional relationship. However, the suspension force component F_y is always close to zero when the eccentric distance in x-axis varies.

Figure 22 illustrates the relationship waveforms of the suspension force and eccentric distance in x-axis, and makes comparisons between the calculated and simulated suspension forces. From Fig. 22,

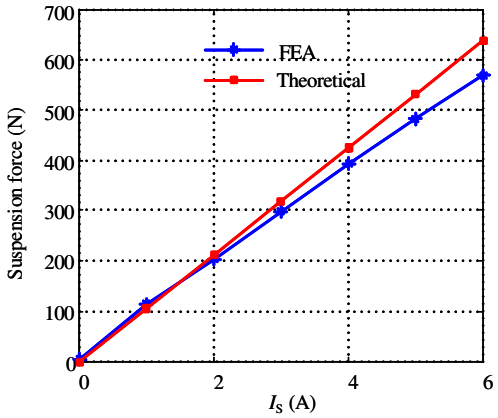

Figure 20. Suspension force versus I_S.

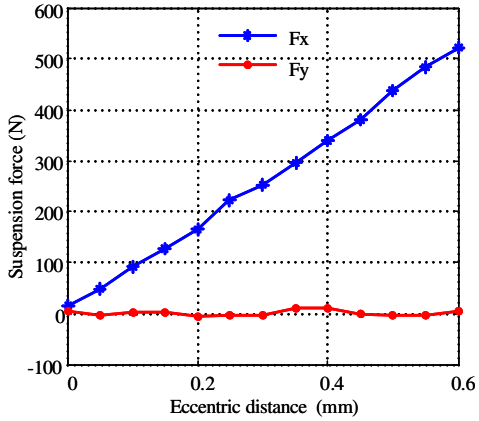

Figure 21. F_x and F_y versus x.

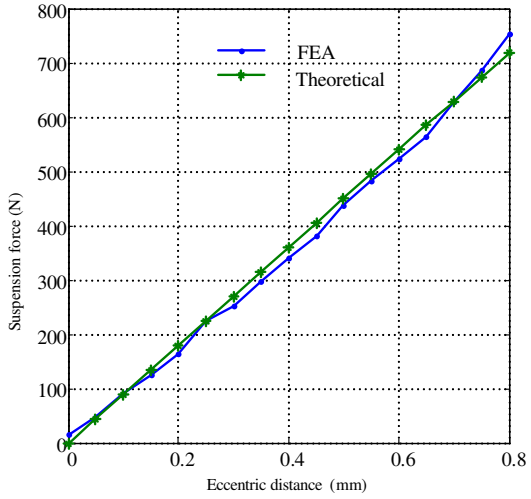

Figure 22. Suspension force versus rotor eccentric distance.

it can be seen that the calculated suspension force is consistent with the simulated one, which can lay an important foundation for the suspension force control.

4. CONCLUSION

In this paper, the mathematical model of the suspension force is built based on the Maxwell tensor method. Then, the magnetic field analysis and static electromagnetic characteristics, including the PM flux linkage, EMF, inductance, electromagnetic torque and suspension force, are analyzed. The results are summarized as follows. Firstly, the third order harmonic has great influence on the PM flux linkage and EMF. Secondly, the inductance is not only affected by the rotor position, but also affected by the effect of the torque winding magnetic field. Thirdly, the cogging torque only produces torque ripple. Finally, the calculated suspension force is very close to the simulated one. These results have reference value for the optimization design and control strategies of the IBPMSM.

ACKNOWLEDGMENT

This work was supported in part by the National Natural Science Foundation of China under Projects 51305170, 51475214, and U1564201, by the National Science Foundation of Jiangsu Province under Projects BK20130515, BK20141301, and BK20150524, by the China Postdoctoral Science Foundation under Project 2015T80508, by the Six Categories Talent Peak of Jiangsu Province under Projects 2015-XNYQC-003 and 2014-ZBZZ-017, and by the Priority Academic Program Development of Jiangsu Higher Education Institutions (PAPD).

REFERENCES

1. Rodriguez, E. F. and J. A. Santisteban, "An improved control system for a split winding bearingless induction motor," *IEEE Transactions on Industrial Electronics*, Vol. 58, 3401–3408, 2011.
2. Huang, J., B. Li, H. Jiang, and M. Kang, "Analysis and control of multiphase permanent-magnet bearingless motor with a single set of half-coiled winding," *IEEE Transactions on Industrial Electronics*, Vol. 61, 3137–3145, 2014.
3. Ichikawa, O., A. Chiba, and T. Fukao, "Inherently decoupled magnetic suspension in homopolar-type bearingless motors," *IEEE Transactions on Industry Applications*, Vol. 37, 1668–1674, 2001.
4. Bartholet, M. T., T. Nussbaumer, D. Krahenbuhl, F. Zurcher, and J. W. Kolar, "Modulation concepts for the control of a two-phase bearingless slice motor utilizing three-phase power modules," *IEEE Transactions on Industry Applications*, Vol. 46, 831–840, 2010.
5. Sun, X., L. Chen, and Z. Yang, "Overview of bearingless permanent-magnet synchronous motors," *IEEE Transactions on Industrial Electronics*, Vol. 60, 5528–5538, 2013.
6. Sun, X., H. Zhu, and Z. Yang, "Nonlinear modeling of flux linkage for a bearingless permanent magnet synchronous motor with modified particle swarm optimization and least squares support vector machines," *Journal of Computational and Theoretical Nanoscience*, Vol. 10, 412–418, 2013.
7. Hiromi, T., T. Katou, A. Chiba, M. A. Rahman, and T. Fukao, "A novel magnetic suspension-force compensation in bearingless induction-motor drive with squirrel-cage rotor," *IEEE Transactions on Industry Applications*, Vol. 43, 66–76, 2007.
8. Chiba, A. and J. Asama, "Influence of rotor skew in induction type bearingless motor," *IEEE Transactions on Magnetics*, Vol. 48, 4646–4649, 2012.
9. Wang, H., J. Liu, J. Bao, and B. Xue, "A novel bearingless switched reluctance motor with a biased permanent magnet," *IEEE Transactions on Industrial Electronics*, Vol. 61, 6947–6955, 2014.
10. Takemoto, M., A. Chiba, and T. Fukao, "A method of determining the advanced angle of square-wave currents in a bearingless switched reluctance motor," *IEEE Transactions on Industry Applications*, Vol. 37, 1702–1709, 2001.
11. Sun, X., L. Chen, Z. Yang, and H. Zhu, "Analysis of inductance characteristics for a bearingless permanent magnet synchronous motor," *Electrical Engineering*, Vol. 95, 277–286, 2013.

12. Miyamoto, N., T. Enomoto, M. Amada, J. Asama, A. Chiba, T. Fukao, S. Iwasaki, and M. Takemoto, "Suspension characteristics measurement of a bearingless motor," *IEEE Transactions on Magnetics*, Vol. 45, 2795–2798, 2009.
13. Sun, X. and H. Zhu, "Study on static electromagnetic characteristics of a bearingless permanent magnet synchronous motor," *Advanced Science Letters*, Vol. 4, 1–9, 2011.
14. Sun, X., L. Chen, Z. Yang, H. Zhu, W. Zuo, and K. Shi, "Modeling of a bearingless permanent magnet synchronous motor considering rotor eccentricity and coupling relationship of windings," *Diangong Jishu Xuebao/Transactions of China Electrotechnical Society*, Vol. 28, 63–70, 2013.
15. Cao, X., Z. Deng, G. Yang, Y. Yang, and X. Wang, "Mathematical model of bearingless switched reluctance motors based on Maxwell stress tensor method," *Zhongguo Dianji Gongcheng Xuebao/Proceedings of the Chinese Society of Electrical Engineering*, Vol. 29, 78–83, 2009.
16. Faiz, J., B. M. Ebrahimi, and M. B. B. Sharifian, "Time stepping finite element analysis of broken bars fault in a three-phase squirrel-cage induction motor," *Progress In Electromagnetics Research*, Vol. 68, 53–70, 2007.
17. Yang, Z. B., R. Jin, X. D. Sun, and W. Y. Zhang, "Study on radial suspension force of single winding bearingless induction motor based on two-fundamental wave method," *Progress In Electromagnetics Research M*, Vol. 47, 13–25, 2016.
18. Pahlavani, M. and H. Omran, "A new analytical description and FEA validation of an effective method to reduce the cogging torque in SM-AFPM motors," *Progress In Electromagnetics Research M*, Vol. 42 189–197, 2015.